Advances in Mechanical Engineering

Research Article

Advances in Mechanical Engineering
2023, Vol. 15(6) 1–16

DOI: 10.1177/16878132231179611
journals.sagepub.com/home/ade
Sage

Mixed convection MHD hybrid nanofluid flow between two parallel rotating discs with joule heating and chemical reactions using bvp4c

Amjid Rashid, Muhammad Ayaz and Saeed Islam

Abstract

Several characteristics of the resulting fluid are influenced by the nanoparticle suspension. Understanding the heat transfer mechanism in nanofluids is necessary for many production and manufacturing applications. The current study examines the effects of mixed convection MHD and Joule heating on the flow of ($TiO_2 - GO$/water) hybrid nanofluid and (TiO_2/water) nanofluids in the porous media between two parallel, infinitely spinning discs when radiation occurs. Using the "bvp4c" function in MATLAB, the governing equations are numerically solved. A graphic is used to show how important parameters affect the velocity, temperature, and concentration of nanoparticles. Finally, a table depicting the interactions between several important factors and skin friction, the Nusselt number, and the Sherwood number at the upper and lower discs is created. The findings show that while the local skin fraction drops with an increase in the mixed convection parameter, the heat transmission rate at both discs increases. Additionally, the rate of heat transmission at both the top and lower discs is reduced as the radiation and magnetic parameters increase. This study's findings will be helpful to numerous nanofluid-based medicinal applications, architectural design systems, better oil recovery systems, and transportation procedures, among other sectors.

Keywords

Mixed convection, joule heating, hybrid nanofluid, MHD flow, chemical reaction, chemical reaction and bvp4c

Date received: 25 January 2023; accepted: 16 May 2023

Handling Editor: Chenhui Liang

Introduction

Hybrid nanofluids are frequently used in experimental and numerical fluid dynamics research due to their importance in thermal and energy performance. Like regular NFs, hybrids NFs are usually created by mixing nanoparticles with common fluids like water, oil, and ethylene glycol. The distinction is that hybrid NFs has a solid phase made up of two or more different kinds of nanoparticles, one of which is commonly graphene, carbon nanotubes, or a nanoparticle with extremely high heat conductivity. Due to the inclusion of two or more different types of particles in hybrid NFs, the fluid's thermal and rheological characteristics alter significantly. The key attributes that change to improve thermal performance as a result of the interaction between various nanoparticles are those related to thermophysics. Abderrahmane et al.[1] investigated the flow of a hybrid nanofluid in a cubic hollow under a magnetic field in three dimensions. The flow of an

Department of Mathematics, Abdul Wali Khan University, Mardan, Khyber Pakhtunkhwa, Pakistan

Corresponding author:
Amjid Rashid, Department of Mathematics, Abdul Wali Khan University, Mardan, Khyber Pakhtunkhwa 23200, Pakistan.
Email: amjidrashid2016@gmail.com

incompressible, viscous, electrically conducting hybrid nanofluid over a vertical surface that is accelerated exponentially was studied by Krishna and Chamkha.[2] The Yamada-Ota model and the Xue model were extended versions that were used to show the magnetohydrodynamic stationary point flow in hybrid nanofluid in Ishtiaq et al.[3] In the temperature range of 5°C–55°C and under various laboratory settings, Esfe et al.[4] examined the rheological behavior of a particular kind of hybrid nanofluid (HNF). Gamachu and Ibrahim[5] investigated the fluid flow, temperature, and entropy formation in a partially heated cavity saturated with porous media for buoyancy-driven flow of hybrid nanofluid. For various physical characteristics and surfaces, such as a moving plate, the investigation of numerical solutions in hybrid nanofluid flow was investigated,[6–12] cylinder,[13–17] disc,[18–23] and thin needle.[24–28]

According to theory, joule heating is the generation of heat as a result of resistive losses during the conversion of electric to thermal state energy. The arrangement of electrical and electronic devices frequently uses this method. According to research by Reddy and Reddy,[29] this control parameter is employed to raise the temperature of the nanofluid from the perspective of boundary layer flow. Maskeen et al.[30] and Khashi'ie et al.[31] examined the impact of Joule heating in Cu-Al_2O_3/water along a stretching and contracting cylinder, respectively. According to Yan et al.[32] and Khashi'ie et al.,[31] the dimensionless Eckert number (derived from the Joule heating) has no effect on prolonging the point of separation. According to Chamkha et al.,[33] MHD hybrid nanofluid flow with Joule heating and thermal radiation between two parallel plates was examined. Li et al.[34] conducted an analysis of the effect of Joule heating on the flow of nanofluid through a permeable conduit. While this was going on, Saranya et al.[35] noticed how the hybrid ferrofluid flow through a contracting cylinder was affected by viscous dissipation and Joule heating. They employ a base fluid mixture of water (50%) and ethylene glycol (50%) along with magnetite-cobalt ferrite hybrid nanoparticles in their study. The combined impact of an angled magnetic field and a radiation parameter on the Marangoni hybrid nanofluid flow was examined by Al-Mdallal et al.[36] The following remarkable articles on the energy transmission of nanofluids were also discussed in Refs.[37–42]

Magnetic fields can induce currents to flow in a mobile conductive fluid, and rotating MHD flows make use of this possibility. Liquid metals, plasmas, and electrolytes are notable examples of MHD fluids. MHD flows can change a number of flow regimes by employing a Lorentzian drag force. The study of MHD flow and its effect on entropy production in related systems has recently received considerable interest due to its importance in many fields.[43–46] In magnetohydrodynamic (MHD) flow on a spinning disc, Arikoglu et al.[47] investigated the impact of slip on the generation of entropy. The mixed convection Darcy-Forchheimer flow of ZnO-SAE50 oil nanolubricant across a rotating disc that was inclined and subject to a uniform magnetic field was studied by Nayak et al.[48] The dynamics of a rotating disc model with a stretchable flow field were investigated by Mehmood et al.[49] Barman et al.[50] investigated the entropy generated and the flow of a radiative magneto-hybrid nanofluid across a spinning sphere. Mahanthesh et al.[51–54] explored a nonlinear radiated MHD flow of nanoliquid generated by a rotating disc with an unequal heat source and heat flux condition.

Since just a few researches have been published to examine the significance of HNF between two spinning discs, it can be concluded from the discussion that came before it. To examine the HNF flow (TiO_2-Go/water flow) and NF flow (TiO_2/water flow) between two parallel, infinitely rotating discs, authors have created a model. Additionally, the significance of mixed convection, joule heating, thermal radiation, magnetic field, and chemical reaction are also researched as a novelty. Additionally, this study seeks to examine the mass transmission rate (MTR) and the HTR of the HNF flow (TiO_2-Go/water flow) and NF flow (TiO_2/water flow) at both discs. The bvp4c solver in MATLAB is used to look for the numerical solution. According to the author's knowledge, no one has ever reported a comparison of the HNF flow (TiO_2-Go/water) and NF flow (TiO_2/water) between two parallel, infinite spinning discs, and the findings are fresh and original.

Problem formulation

Consider the axisymmetric, incompressible, and steady three-dimensional flow of the hybrid nanofluid ($TiO_2 - GO$/water) and nanofluid (GO/water) between the two spinning infinite discs (see Figure 1). For the cylindrical coordinate system, the notation (r, θ, z) has been employed (see Figure 1). In the z-direction, a magnetic field B_0 is present and exposed to the flow. Mixed convection and joule heating are utilized as a new porous medium in the development of the model. Thermal radiation is additionally utilized to study hybrid nanofluid transcends (HTR) and mass transfer rate (MTR). The chemical reaction is also represented by the final term in the concentration equation (equation (6)).The lower and upper disc are placed at $z = 0$ and $z = h$ (see equation (7)). The lower and upper discs' radial shrinkage rates are A_1 and A_2 which represented in the boundary conditions. Additionally, the angular velocities of the bottom and higher discs, respectively, are assumed to be Ω_1 and Ω_2. It is considered that hot liquids with surface temperatures T_1 (lower disc) and away from the surface, temperature T_2 (upper disc) with a heat

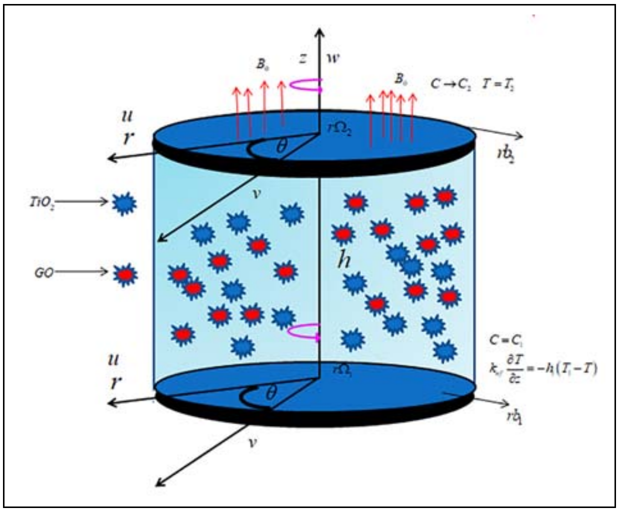

Figure 1. Flow sketch.

Table 1. Titanium di oxide and graphene oxide thermophysical characteristics with ordinary fluid water.[55,58]

Properties	$k(w/mK)$	$\sigma(Um)^{-1}$	$c_p(J/kgK)$	$\rho(kg/m^3)$
Titanium di oxide (TiO_2)	8.9538	$2.6e^6$	686.2	4250
Graphene oxide (GO)	5000	$1.1e^{-5}$	717	1800
Water (H_2O)	0.613	0.05	4179	997.1

Table 2. Thermophysical models of hybrid nanofluids.[55–59]

Properties	Hybrid nanofluid
Density	$\rho_{hnf} = \rho_f(1-\phi_b)(1-\phi_a) + \phi_a\rho_{sa} + \phi_b\rho_{sb}$.
viscosity	$\mu_{hnf} = \frac{\mu_f}{(1-\phi_a)^{2.5}(1-\phi_b)^{2.5}}$.
Heat capacity	$(\rho c_p)_{hnf} = (\rho c_p)_f(1-\phi_b)\left((1-\phi_a) + \frac{\phi_a(\rho c_p)_{sa}}{(\rho c_p)_f}\right) + \phi_b(\rho c_p)_{sb}$.
Thermal conductivity ratio	$\frac{k_{hnf}}{k_{bf}} = \left(\frac{(k_{sb}+2k_{bf}) - 2\phi_b(k_{bf}-k_{sb})}{(k_{sb}+2k_{bf}) + \phi_b(k_{bf}-k_{sb})}\right)$ where $\frac{k_{bf}}{k_f} = \frac{k_{sa}+2k_f-2\phi_a(k_f-k_{sa})}{k_{sa}+2k_f+\phi_a(k_f-k_{sa})}$
Electrical conductivity ratio	$\frac{\sigma_{hnf}}{\sigma_{bf}} = \left(\frac{\sigma_{sb}+2\sigma_{bf}-2\phi_b(\sigma_{bf}-\sigma_{sb})}{\sigma_{sb}+2\sigma_{bf}+\phi_b(\sigma_{bf}-\sigma_{sb})}\right)$ where $\frac{\sigma_{bf}}{\sigma_f} = \frac{\sigma_{sa}+2\sigma_f-2\phi_a(\sigma_f-\sigma_{sa})}{\sigma_{sa}+2\sigma_f+\phi_a(\sigma_f-\sigma_{sa})}$.
Buoyancy coefficient	$(\rho\beta)_{hnf} = (\rho\beta)_f(1-\phi_b)(1-\phi_a) + \phi_a(\rho\beta)_{sa} + \phi_b(\rho\beta)_{sb}$.

transfer coefficient of h_1 (lower disc) are convectively heating the outer surfaces of the discs. C_1 and C_2 also stand for the concentration of NPs at the lower and upper discs, respectively. The (r, θ, z) cylindrical coordinate system is used to create the following mathematical model.[52–54]

$$\frac{\partial u}{\partial r} + \frac{u}{r} + \frac{\partial w}{\partial z} = 0, \tag{1}$$

$$u\frac{\partial u}{\partial r} + w\frac{\partial u}{\partial z} - \frac{v^2}{r} = -\frac{1}{\rho_{hnf}}\frac{\partial p}{\partial r} + \nu_{hnf}\left(\frac{\partial^2 u}{\partial r^2} + \frac{1}{r}\frac{\partial u}{\partial r} + \frac{\partial^2 u}{\partial z^2} - \frac{u}{r^2}\right) - \frac{\sigma_{hnf}}{\rho_{hnf}}B_0^2 u + \frac{(\rho\beta)_{hnf}}{\rho_{hnf}}g(T-T_\infty), \tag{2}$$

$$u\frac{\partial v}{\partial r} + w\frac{\partial v}{\partial z} + \frac{uv}{r} = \nu_{hnf}\left(\frac{\partial^2 v}{\partial r^2} + \frac{1}{r}\frac{\partial v}{\partial r} + \frac{\partial^2 v}{\partial z^2} - \frac{v}{r^2}\right) - \frac{\sigma_{hnf}}{\rho_{hnf}}B_0^2 v, \tag{3}$$

$$u\frac{\partial w}{\partial r} + w\frac{\partial w}{\partial z} = -\frac{1}{\rho_{hnf}}\frac{\partial p}{\partial z} + \nu_{hnf}\left(\frac{\partial^2 w}{\partial r^2} + \frac{1}{r}\frac{\partial w}{\partial r} + \frac{\partial^2 w}{\partial z^2}\right), \tag{4}$$

$$\left(u\frac{\partial T}{\partial r} + w\frac{\partial T}{\partial z}\right) = \frac{1}{(\rho c_p)_{hnf}}\left(k_{hnf} + \frac{16\sigma^0 T_2^3}{3k^0}\right)\left(\frac{1}{r}\frac{\partial T}{\partial r} + \frac{\partial^2 T}{\partial r^2} + \frac{\partial^2 T}{\partial z^2}\right) + \frac{\sigma_{hnf}}{(\rho c_p)_{hnf}}B_0^2(u^2+v^2), \tag{5}$$

$$u\frac{\partial C}{\partial r} + w\frac{\partial C}{\partial z} = D\left(\frac{\partial^2 C}{\partial r^2} + \frac{1}{r}\frac{\partial C}{\partial r} + \frac{\partial^2 C}{\partial z^2}\right) - k_1(C - C_\infty), \tag{6}$$

$$\left\{\begin{array}{l} u = b_1 r,\ v = r\Omega_1,\ w = 0,\ k_{hnf}\frac{\partial T}{\partial z} = -h_1(T_1 - T), \\ \quad C = C_1, \quad \text{at lower disk } z = 0, \\ u = b_2 r,\ v = r\Omega_2,\ w = 0,\ T = T_2, \quad C \to C_2, \\ \quad \text{at upper disk } z = h, \end{array}\right\} \tag{7}$$

where r and θ are the radial and tangential axes of the cylindrical system, respectively, and z is its vertical axis. p denotes pressure, T denotes temperature, T_1 and T_2 denote lower and upper disc temperatures, respectively, and k_0^* is the mean absorption coefficient and σ_0^* stefan Boltzmann constant (Table 1).

The effective hybnanofluids density ρ_{hnf}, k_{hnf} thermal conductivity, $(\rho c_p)_{hnf}$ heat capacitance, μ_{hnf} dynamic viscosity, and σ_{hnf} electrical conductivity can be introduced as follow (Table 2):

Here β_T, k, C_p, v, μ, ρ, ϕ_a, ϕ_b, σ, sa, sb, f and hnf are thermal expansion coefficient, thermal conductivity, specific heat, dynamic viscosity, density, nanoparticle volume fraction of first nanoparticle, nanoparticle volume fraction of second nanoparticle, electric conductivity, first solid nanoparticle, second solid nanoparticles, base fluid, and hybrid nanofluid, respectively.

It is taken into consideration though using the Karman transformation:

$$\left\{\begin{array}{l} u = r\Omega_1 f'(\xi),\ v = r\Omega_1 g(\xi),\ w = -2h\Omega_1 f(\xi),\ \theta = \dfrac{T-T_2}{T_1-T_2} \\ p = \rho_f \Omega_1 \nu_f \left(p(\xi) + \dfrac{1}{2}\dfrac{r^2}{h^2}\varepsilon\right),\ \phi = \dfrac{C-C_2}{C_1-C_2},\ \xi = \dfrac{z}{h} \end{array}\right\} \tag{8}$$

Using equation (8) the governing non-linear partial differential equations (1)–(6) together with the boundary conditions (7) reduce to

The continuity equation is satisfied and other equations (2)–(6) are transformed to:

$$\frac{Z_1}{Z_2}f''' + \mathrm{Re}\left(2ff'' - f'^2 + g^2\frac{Z_3}{Z_2}Mf'\right) - \frac{\varepsilon}{Z_2} + \frac{Z_6}{Z_2}Ri.\theta = 0, \tag{9}$$

$$\frac{Z_1}{Z_2}g'' + \mathrm{Re}\left(2fg' - 2f'g - M\frac{Z_3}{Z_2}g\right) = 0, \tag{10}$$

$$P'(\xi) + 4\frac{Z_2}{Z_3}\mathrm{Re}ff' + 2f'' = 0, \tag{11}$$

$$\frac{1}{\mathrm{Pr}}(Z_5 + R)\theta'' + 2\mathrm{Re}Z_2 f\theta' + Ec\mathrm{Re}MZ_3\left(f'^2 + g^2\right) = 0, \tag{12}$$

$$\phi'' + 2Sc\mathrm{Re}f\phi' - ScCr\phi = 0, \tag{13}$$

Where,

$$\left\{Z_1 = \frac{\mu_{hnf}}{\mu_f},\ Z_2 = \frac{\rho_{hnf}}{\rho_f},\ Z_3 = \frac{\sigma_{hnf}}{\sigma_f},\ Z_4 = \frac{(\rho c_p)_{hnf}}{(\rho c_p)_f},\ Z_5 = \frac{k_{hnf}}{k_f},\ Z_6 = \frac{(\rho\beta)_{hnf}}{\rho_f\beta_f}\right\}$$

The transfer boundary conditions are

$$\left\{\begin{array}{l} f(0) = 0, f(1) = 0, f'(0) = A_1, f'(1) = A_2,\ g(0) = 1, \\ \quad g(1) = \Omega,\ \phi(0) = 1, \\ \theta'(0) = -\dfrac{1}{Z_5}B_1(1-\theta(0)),\quad \theta(1) = 0,\quad \phi(1) = 0, \end{array}\right\} \tag{14}$$

$$\left\{\begin{array}{l} \mathrm{Re} = \dfrac{\Omega_1 h^2}{\nu_f}, M = \dfrac{B_0^2\sigma_f}{\rho_f\Omega_1}, \mathrm{Pr} = \dfrac{(\rho c_p)_f\nu_f}{k_f}, Ec = \dfrac{r^2\Omega_1^2}{(c_p)_f(T_1-T_2)}, \\ \quad Cr = \dfrac{K_1 h^2}{\nu_f} \\ Sc = \dfrac{\nu_f}{D}, A_1 = \dfrac{a_1}{\Omega_1}, A_2 = \dfrac{a_2}{\Omega_1}, \Omega = \dfrac{\Omega_2}{\Omega_1}, B_1 = \dfrac{hh_1}{k_f}, \\ \quad Ri = \dfrac{Gr}{\mathrm{Re}^2}, Gr = \dfrac{g\rho_f\beta_f(T_1-T_2)h^3}{\nu_f{}^2} \end{array}\right\}$$

where Ri stand for mixed convection, Re stands for Reynolds number, Gr expresses the Grashof number, Pr stands for Prandtl number, M stand for magnetic field, Sc stands for Schmidt number, scaled stretching parameters A_1 and A_2, and Ω stand for rotation number, respectively. The diffusion coefficients of Chemical species Cr and B_1 convective parameter.

For making simpler form of equation (9) and removing ε, it can be differentiated with respect to ξ

$$\frac{Z_1}{Z_2}f^{iv} + \mathrm{Re}\left(2ff''' - 2gg' - M\frac{Z_3}{Z_2}f''\right) = 0, \tag{15}$$

Equations (9)–(14) defined the ε (pressure variable) as follow:

$$\varepsilon = Z_1 f'''(0) + \mathrm{Re}Z_2\left(2f(0)f''(0) - f'^2(0) + g^2(0)\frac{Z_3}{Z_2}Mf'(0)\right) + Z_6 Ri.\theta(0), \tag{16}$$

For pressure, solve equation (11) by taking integration from 0 to ξ and obtained this form:

$$P = -2\left\{f'(\xi) - f'(0) + \frac{Z_2}{Z_1}\mathrm{Re}f^2(\xi)\right\} = 0 \tag{17}$$

At lower disc the shear stress in radial and tangential direction is described by:

$$\tau_{zr} = \mu_{nf}\left.\frac{\partial u}{\partial z}\right|_{z=0} = \frac{\mu_f r\Omega_1 f''(0)}{(1-\phi)^{2.5}h},\ \tau_{z\theta} = \mu_{nf}\left.\frac{\partial v}{\partial z}\right|_{z=0} = \frac{\mu_f r\Omega_1 g'(0)}{(1-\phi)^{2.5}h}, \tag{18}$$

Therefore total difference is defined as:

$$\tau_w = \sqrt{\tau_{zr}{}^2 + \tau_{z\theta}{}^2}, \tag{19}$$

The skin fraction coefficients Cf_1 and Cf_2 in lower and upper discs is illustrated by:

$$Cf_1 = \frac{\tau_w|_{z=0}}{\rho_f(r\Omega_1)^2} = \frac{1}{\mathrm{Re}_r(1-\phi)^{2.5}}\left[(f''(0))^2 + (g'(0))^2\right]^{1/2}, \tag{20}$$

$$Cf_2 = \frac{\tau_w|_{z=h}}{\rho_f(r\Omega_1)^2} = \frac{1}{\mathrm{Re}_r(1-\phi)^{2.5}}\left[(f''(1))^2 + (g'(1))^2\right]^{1/2}, \tag{21}$$

In which local Reynolds number $\mathrm{Re}_x = \dfrac{r\Omega_1 h}{\nu_f}$

Nusselt number for lower and upper discs can be expressed as:

$$Nu_{x1} = \left.\frac{hq_w}{k_f(T_1-T_2)}\right|_{z=0},\quad Nu_{x2} = \left.\frac{hq_w}{k_f(T_1-T_2)}\right|_{z=h}, \tag{22}$$

In which surface heat flux is

$$q_w|_{z=0} = -k_{nf}\frac{\partial T}{\partial z} + q_r|_{z=0} = -\frac{(T_1-T_2)}{h}\left(k_{nf} + \frac{16\sigma_0 T_2^3}{3k^0}\right)\theta'(0), \tag{23}$$

$$q_w|_{z=h} = -k_{nf}\frac{\partial T}{\partial z} + q_r|_{z=h} = -\frac{(T_1 - T_2)}{h}\left(k_{nf} + \frac{16\sigma_0 T_2^3}{3k^0}\right)\theta'(1), \tag{24}$$

Therefore Nusselt number can be written as:

$$Nu_{x1} = -B_1[Z_5 + R]\theta'(0),\ Nu_{x2} = -B_1[Z_5 + R]\theta'(1). \tag{25}$$

Sherwood numbers for lower and upper discs can be expressed as

$$Sh_{x1} = \frac{J_w}{D(C_1 - C_2)}\bigg|_{z=0},\ Sh_{x2} = \frac{J_w}{D(C_1 - C_2)}\bigg|_{z=h} \tag{26}$$

In which J_w is surface mass flex is

$$J_m|_{z=0} = -D\frac{\partial C}{\partial z}\bigg|_{z=0},\ J_m|_{z=h} = -D\frac{\partial C}{\partial z}\bigg|_{z=h} \tag{27}$$

$$Sh_{x1} = -\phi'(0),\ Sh_{x2} = -\phi'(1) \tag{28}$$

Appendix solution methodology

In this section of the paper, we demonstrate the mathematical approach of the investigated numerical scheme in detail, as well as the accuracy of the code for the given flow problems. After applying the similarity variables, the updated similarity set of ordinary differential equations (9)–(13) and the boundary condition (15) take on a highly nonlinear form that is very challenging to solve analytically. Thus, using a finite difference approach known as bvp4c, the following numbers of highlighted equations are approximately solved.[60–62]

$$\left\{\begin{array}{l} f(\xi) = u(1),\ f'(\xi) = u(2),\ f''(\xi) = u(3),\ f'''(\xi) = u(4), \\ \quad f^{iv}(\xi) = u'(4), \\ g(\xi) = u(5),\ g'(\xi) = u(6),\ g''(\xi) = u'(6),\ \theta(\xi) = u(7), \\ \quad \theta'(\xi) = u(8), \\ \theta''(\xi) = u'(8),\ \phi(\xi) = u(9),\ \phi'(\xi) = u(10),\ \phi''(\xi) = u'(10), \end{array}\right\} \tag{29}$$

$$\left.\begin{array}{l} f'(\xi) = u(2) \\ u'(2) = u(3) \\ u'(3) = u(4) \\ u'(4) = \frac{Z_1}{Z_2}\left(-\mathrm{Re}u(1)u(4) - 2\mathrm{u}(5)u(6) - \mathrm{M}\frac{Z_3}{Z_2}u(3) - Z_6 Riu(8)\right), \\ u'(5) = u(6) \\ u'(6) = \frac{Z_1}{Z_2}\left(-2\mathrm{Re}u(1)u(6) - 2\mathrm{u}(2)u(5) - \mathrm{M}\frac{Z_3}{Z_2}u(5)\right), \\ u'(7) = u(8) \\ u'(8) = \frac{\mathrm{Pr}}{(Z_5 + Rd)}(-2\mathrm{Z}_4\mathrm{Re}u(1)u(8)) - \mathrm{Re}EcMZ_3\left(u(2)^2 + u(2)^2\right), \\ u'(9) = u(10) \\ u'(10) = -2\mathrm{ScRe}u(1)u(10) - CrScu(9), \end{array}\right\} \tag{30}$$

With boundary condition

$$\left\{\begin{array}{l} u_a(1) = 0,\ u_a(2) = \mathrm{A}_1,\ u_b(1) = 0,\ u_b(1) = \mathrm{A}_2, \\ \quad \mathrm{u}_a(5) = 1,\ u(5) = \Omega, \\ u_a(8) = -\frac{\mathrm{B}_1}{\mathrm{Z}_5}(1 - \mathrm{u}_a(7)),\ \mathrm{u}_b(7) = 0,\ u_a(9) = 1, \\ \quad u_b(9) = 0 \end{array}\right\} \tag{31}$$

Results and discussion

This section focuses on the numerical outcomes and graphical and tabular results are interpreted physically. Authors have used the following general values in the numerical computations: $\mathrm{Pr} = 6.2, M = \mathrm{Re} = Sc = Ec = Cr = Rd = 1, B_1 = 0.5, A_1 = A_2 = \Omega = 1.5$ and $\varphi_1 = \varphi_2 = 0.3$. The analysis is performed for magnetic parameter $(1 \leqslant M \leqslant 3)$, Reynolds numbers $(1 \leqslant \mathrm{Re} \leqslant 3)$, Schmidt number $(1 \leqslant Sc \leqslant 3)$, Eckert number $(1 \leqslant Ec \leqslant 3)$, Mixed convection parameter $(1 \leqslant Ri \leqslant 3)$, chemical reaction parameter $(1 \leqslant Cr \leqslant 3)$, thermal radiation parameter $(1 \leqslant Rd \leqslant 3)$, convective parameter $(0.5 \leqslant B_1 \leqslant 0.7)$, nanoparticle volume fraction $(0.3 \leqslant \varphi \leqslant 0.9)$, and rotation parameter $(1.5 \leqslant \Omega \leqslant 1.7)$. The effect numerous parameter on velocity profile, temperature profile, and concentration profile of hybrids nanofluid $(TiO_2 - GO)/$water and nanofluid TiO_2/water is graphically represented. The effect of the magnetic field parameter M on axial velocity of hybrids nanofluid $(TiO_2 - GO)$/water and nanofluid TiO_2/water is depicted in Figure 2. It can be seen in the figure that the velocity profile exhibits a declining trend. Physically, the Lorentz force, which is what provides resistance to liquid motion and causes axial velocity decay, increases with the value of the M. Figure 3 depicts how the magnetic field M affects radial velocity $F'(\xi)$ of hybrids nanofluid $(TiO_2 - GO)$/water and nanofluid TiO_2/water. As the value increases, a similar pattern emerges. In terms of physics, as

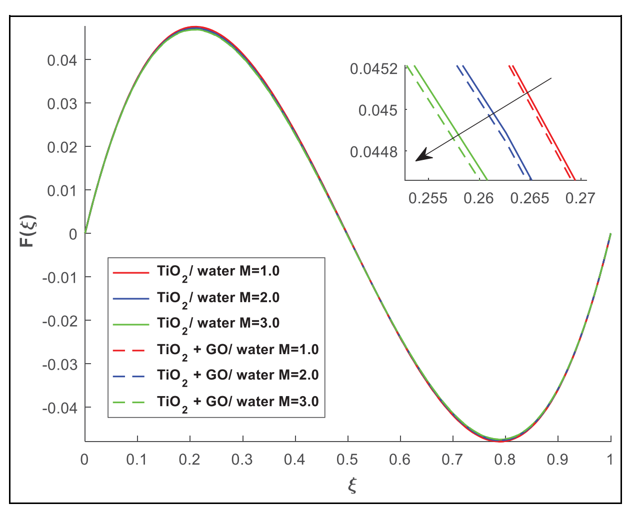

Figure 2. The impact of M over $F(\xi)$.

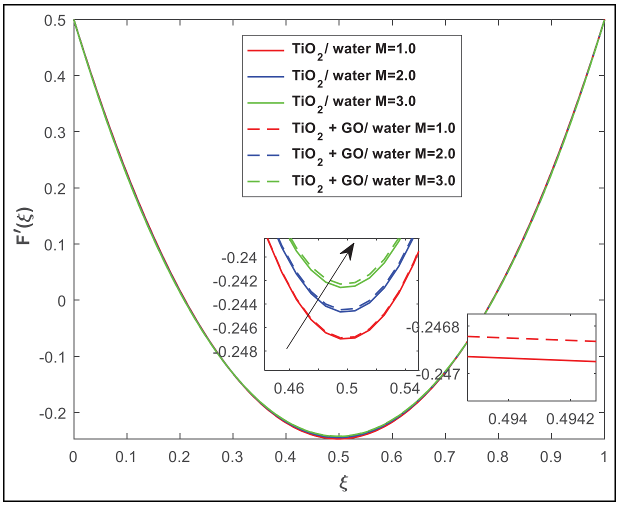

Figure 3. The impact of M over $F'(\xi)$.

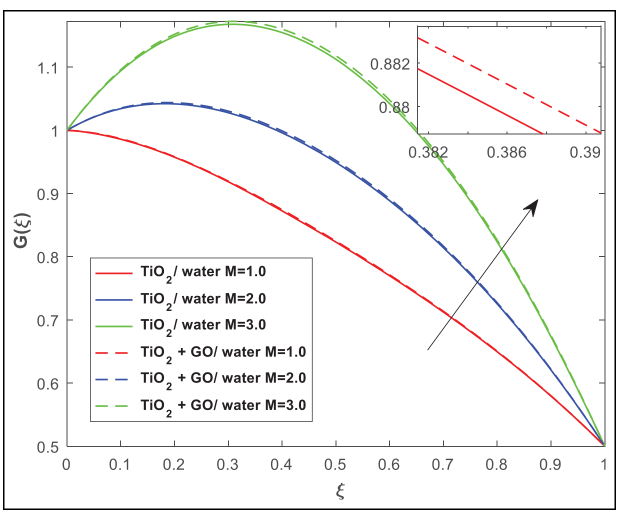

Figure 4. The impact of M over $G(\xi)$.

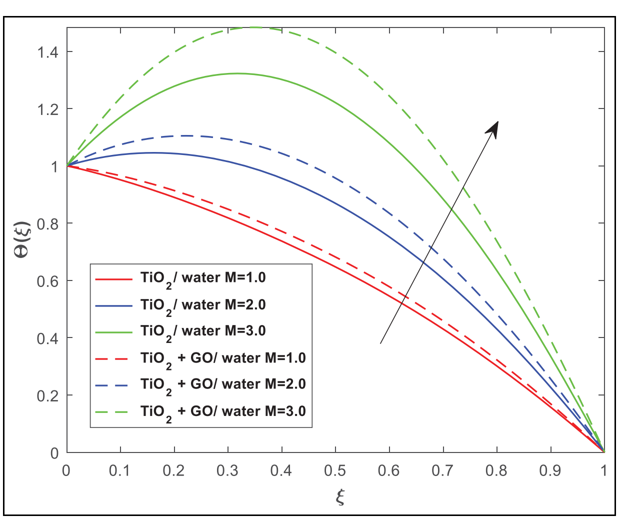

Figure 5. The impact of M over $\theta(\xi)$.

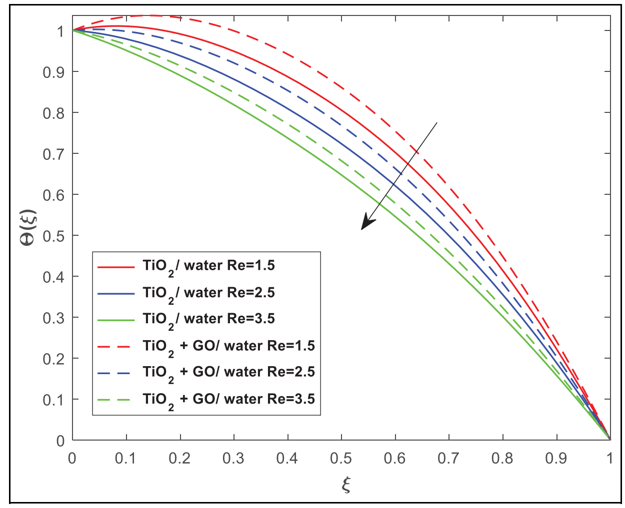

Figure 6. The impact of Re over $\theta(\xi)$.

increases, the momentum boundary layer's radial thickness drops and the thermal boundary layer of the flow thickens. The effect of the magnetic field M on tangential velocity $G(\xi)$ of hybrids nanofluid (TiO_2-GO)/water and nanofluid TiO_2/water is depicted in Figure 4. With a higher value of M, $G(\xi)$ has a stronger impact. By physically decreasing the thickness of the momentum boundary layer in the tangential direction, raising the thermal boundary layer of flow increases the M. Therefore, the $G(\xi)$ displayed rising behavior as the thermal boundary layer expanded in the tangential direction. The effect of magnetic parameters M on the temperature profile $\theta(\xi)$ of hybrids nanofluid (TiO_2-GO)/water and nanofluid TiO_2/water is depicted in Figure 5. A higher value of M is seen to improve the $\theta(\xi)$. Physically, as M rises, the resistance of fluid particles rises as well, raising the $\theta(\xi)$. The effect of the Reynolds number Re on the temperature profile $\theta(\xi)$ of hybrids nanofluid (TiO_2-GO)/water and nanofluid TiO_2/water is depicted in Figure 6. It is clear that the $\theta(\xi)$ decreases as the Re increases. Physically, the thickness of the thermal boundary layer decreases as Re increases. The effect of the Re on tangential velocity $G(\xi)$ of hybrids nanofluid (TiO_2-GO)/water and nanofluid TiO_2/water is depicted in Figure 7. It has been found that a higher value of Re causes them $G(\xi)$ to increase. Physically, bigger Re makes sure that the frequency of harsh collisions declines and that less resistance to liquid motion is offered. Figure 8 depicts the influence of Schmidt number Sc on the concentration field $\psi(\xi)$ of hybrids nanofluid (TiO_2-GO)/water and nanofluid TiO_2/water. With an increase in the Sc, a decrease in the $\psi(\xi)$ is seen because of a decrease in mass diffusivity. Figure 9 shows how the radiation parameter Rd affects the temperature field $\theta(\xi)$ of hybrids nanofluid (TiO_2-GO)/water and nanofluid

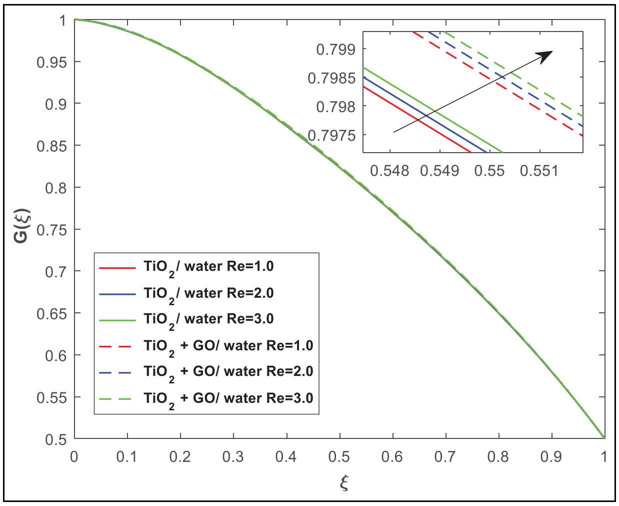

Figure 7. The impact of Re over $G(\xi)$.

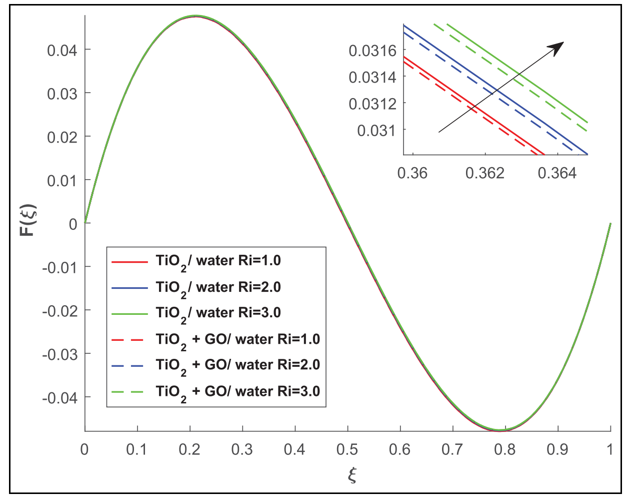

Figure 10. The impact of *Ri* over $F(\xi)$.

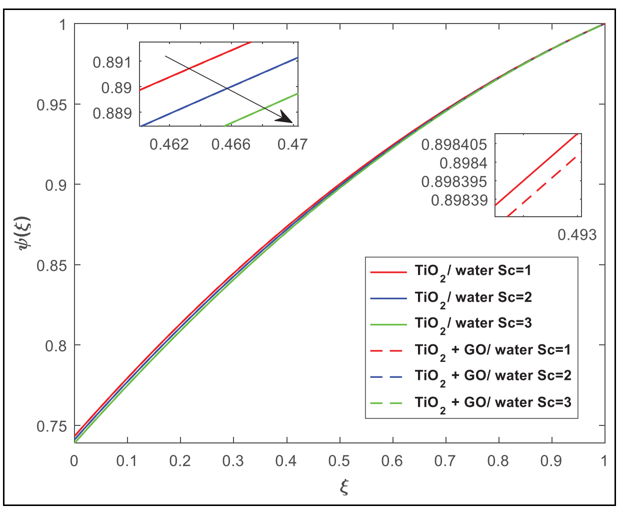

Figure 8. The impact of *Sc* over $\psi(\xi)$.

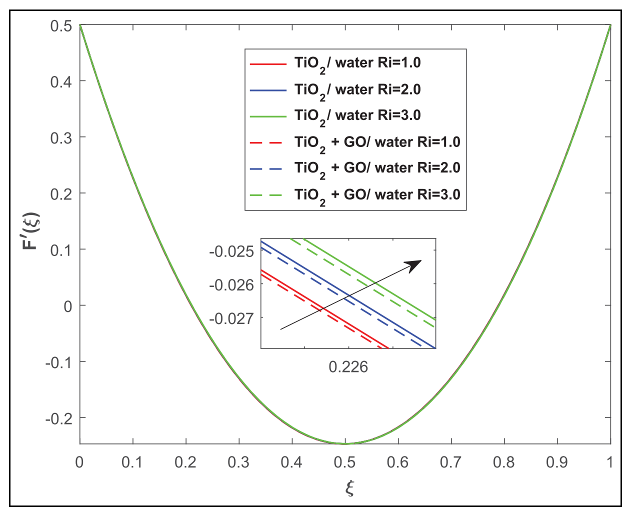

Figure 11. The impact of *Ri* over $F'(\xi)$.

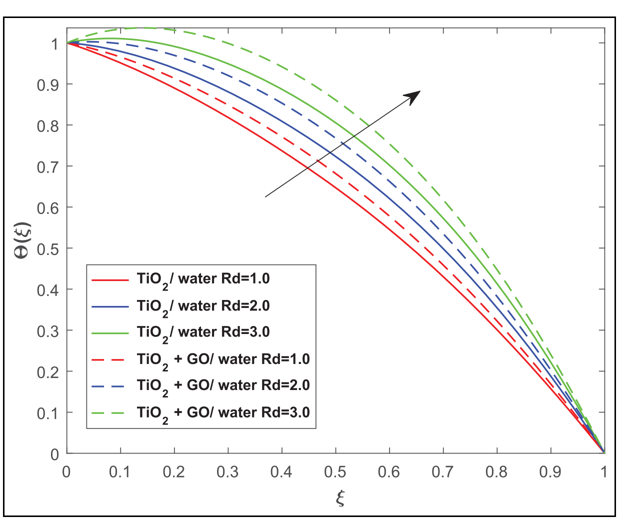

Figure 9. The impact of *Rd* over $\theta(\xi)$.

TiO_2/water. The temperature-increasing tendency is depicted in this figure. Since the ratio of conduction heat transfer to thermal radiation is the Rd. Therefore, it follows that rising Rd temperature causes them $\theta(\xi)$ to rise, as is clear. The distribution of the mixed convection Ri over the profile of $F(\xi)$, radial $F'(\xi)$, and tangential $G(\xi)$ velocities of hybrids nanofluid (TiO_2-GO)/water and nanofluid TiO_2/water is shown in Figures 10 to 12. Physically, Ri increases fluid $F(\xi)$ while reducing boundary layer thickness. Because of forces and pressure, convection causes the fluid density to drop, which causes the fluid's particles to flow. The fluid velocities in the boundary layer region also tend to increase with an increase in the values of Ri. It is obvious that Ri is the buoyancy to inertial forces ratio. Therefore, a rise in the Ri values leads to an increase in the buoyant forces in the boundary layer region, which quickens the flow of fluid. The effects of Ri on the

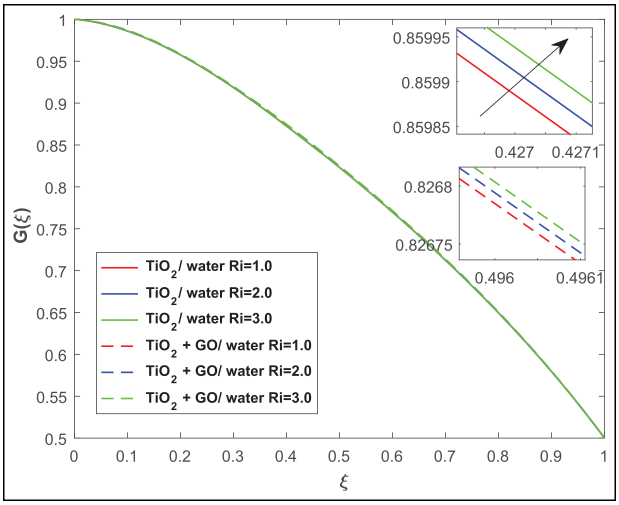

Figure 12. The impact of *Ri* over $G(\xi)$.

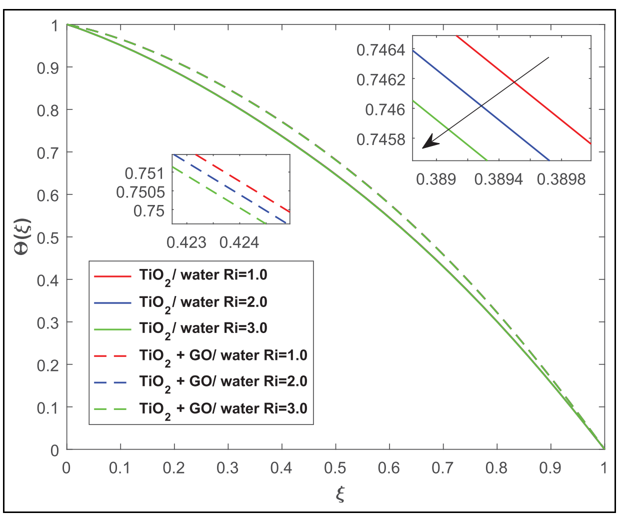

Figure 13. The impact of *Ri* over $\theta(\xi)$.

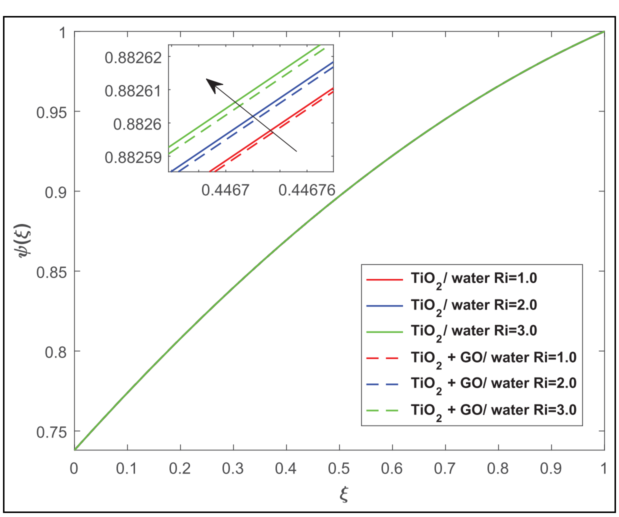

Figure 14. The impact of *Ri* over $\psi(\xi)$.

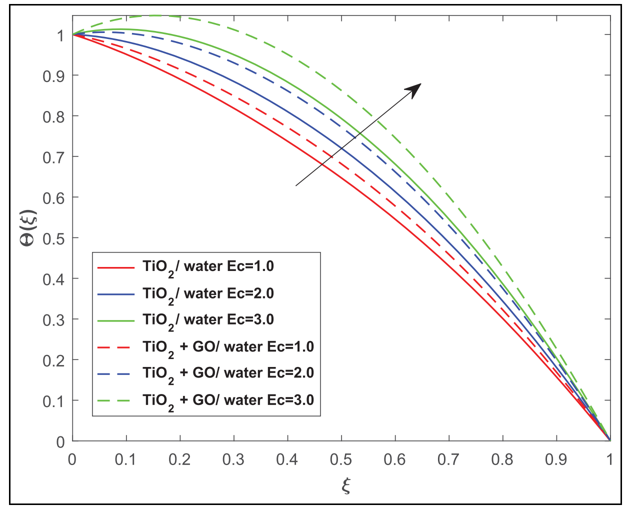

Figure 15. The impact of *Ec* over $\theta(\xi)$.

temperature $\theta(\xi)$ and concentration profile $\psi(\xi)$ of hybrids nanofluid (TiO_2-GO)/water and nanofluid TiO_2/water are depicted in Figures 13 and 14. It is obvious that *Ri* has a decreasing effect on $\theta(\xi)$ and an increasing effect on $\psi(\xi)$. The rate of heat transfer is really accelerated by an increase in the values of the mixed convection parameter in the flow region, which causes buoyant forces to dominate inertial forces. A $\theta(\xi)$ and its boundary layer thickness grow up decreasing as a result. Additionally, a weaker buoyancy force is applied to concentration growth due to its support of the pressure gradient. The effect of the Eckert number *Ec* on the temperature profile $\theta(\xi)$ of hybrids nanofluid (TiO_2-GO)/water and nanofluid TiO_2/water is shown in Figure 15. It is obvious that temperature increases with *Ec*. *Ec* is a crucial physical variable for analyzing the thermal behavior of the fluid flow. The outcome (Figure 15) demonstrates that as the *Ec* rises, the temperature distribution within the boundary layer does as well. As a result, the heat dissipation decreases, and the thermal boundary layer thickens. The effect of chemical reaction parameters *Cr* on the concentration profile $\psi(\xi)$ of hybrids nanofluid (TiO_2-GO)/water and nanofluid TiO_2/water is depicted in Figure 16. The figure makes it very evident that a higher value of *Cr* raises the $\psi(\xi)$. Chemical molecular diffusivity physically decreases with increasing *Cr* due to its consumption in the process. Additionally, as the *Cr* parameter grows, the number of solute molecules performing *Cr* rises as well, which causes a drop in the $\psi(\xi)$. Thus, a destructive *Cr* significantly reduces the thickness of the solutal boundary layer. This result and Chamkha[62] are nearly identical. The effect of the stretching ratio parameter on the profile of axial $F(\xi)$, radial $F'(\xi)$, and tangential $G(\xi)$ velocities of hybrids nanofluid (TiO_2-GO)/water and nanofluid TiO_2/water is depicted in Figures 17 to 19.

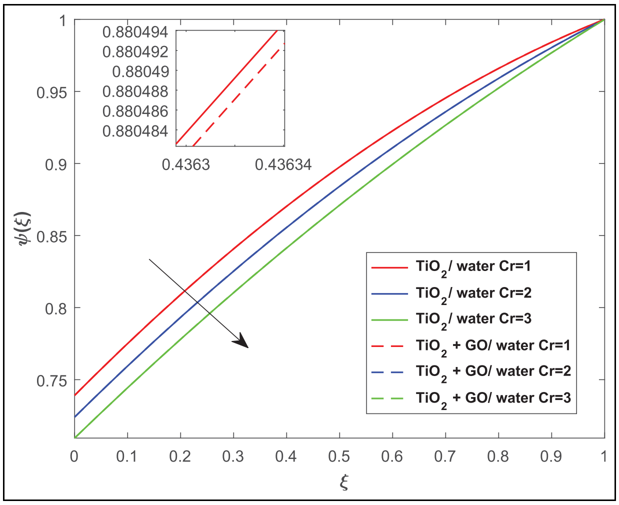

Figure 16. The impact of Cr over $\psi(\xi)$.

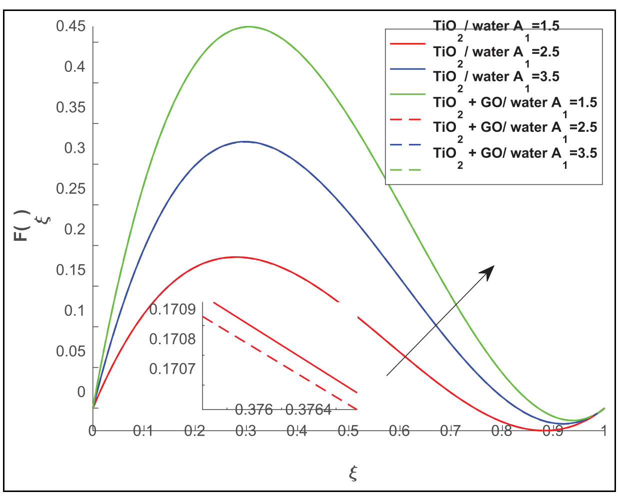

Figure 17. The impact of A_1 over $F(\xi)$.

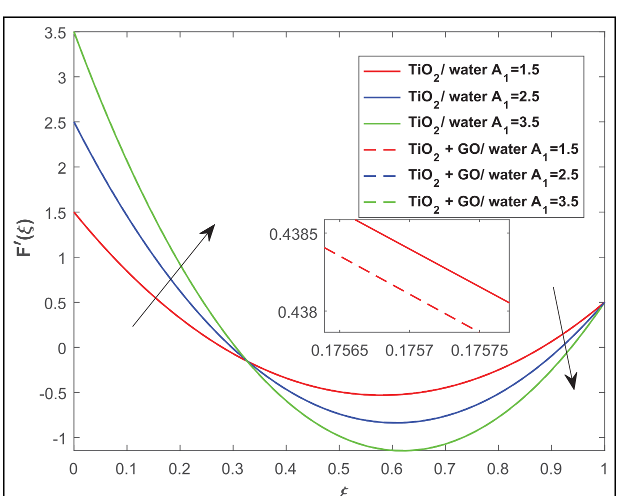

Figure 18. The impact of A_1 over $F'(\xi)$.

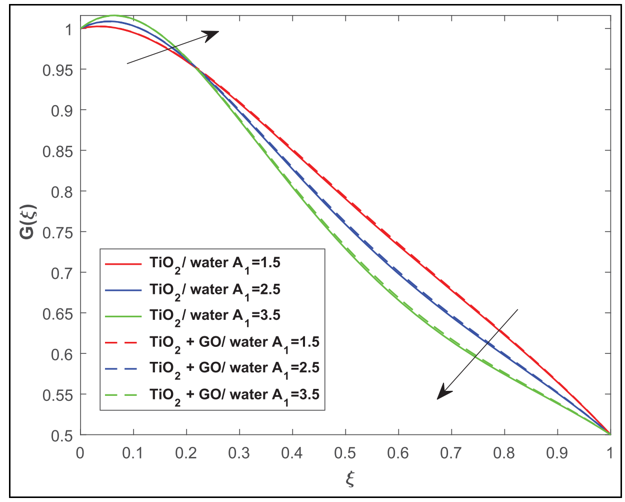

Figure 19. The impact of A_1 over $G(\xi)$.

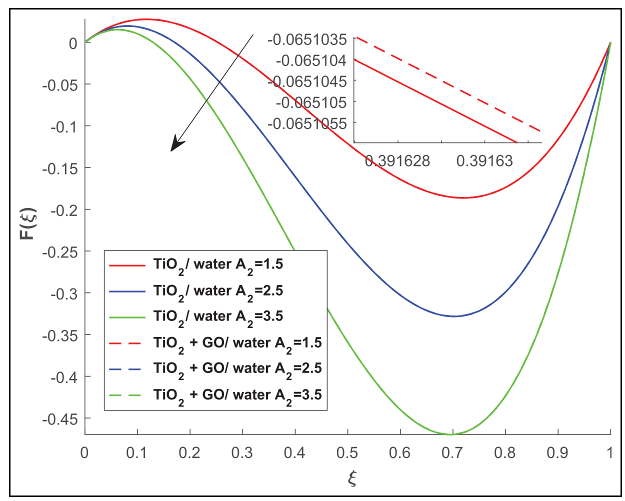

Figure 20. The impact of A_2 over $F(\xi)$.

It has been found that higher values of A_1 improve velocity profiles. Physically, when A_1 rises, the surface of the disc is stretched more. With an increasing amount of A_1, the $F'(\xi)$ and $G(\xi)$ velocities exhibit dual behavior. The effect of the stretching ratio parameter on the profile of axial $F(\xi)$, radial $F'(\xi)$, and tangential $G(\xi)$ velocities of hybrids nanofluid (TiO_2-GO)/water and nanofluid TiO_2/water is depicted in Figures 20 to 22. It has been shown that the velocity profiles fall as A_2 increases. Physically, as A_2 rises, the higher disc gets more stretching force while the lower disc gets less. With an increasing amount of A_2, the $F'(\xi)$ and $G(\xi)$ velocities exhibit dual behavior. The effects of the rotation parameter Ω on the temperature profile $\theta(\xi)$ and concentration profiles $\psi(\xi)$ of hybrids nanofluid (TiO_2-GO)/water and nanofluid TiO_2/water are depicted in Figures 23 and 24. The Ω values that are increasing indicate a larger impact on both profiles. Physically, rising value of the Ω, results

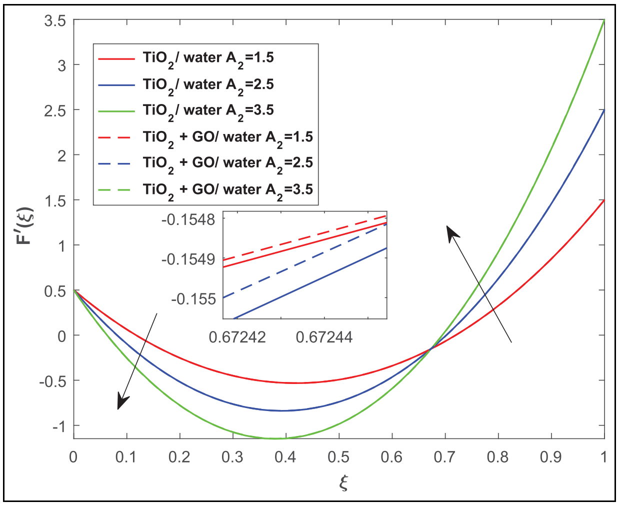

Figure 21. The impact of A_2 over $F'(\xi)$.

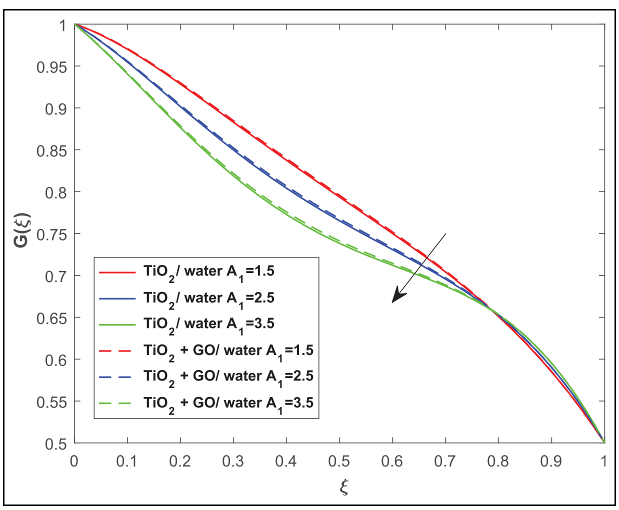

Figure 22. The impact of A_1 over $G(\xi)$.

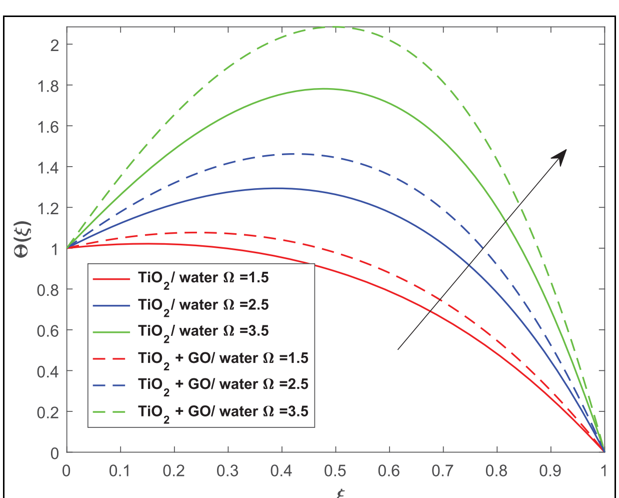

Figure 23. The impact of Ω over $\theta(\xi)$.

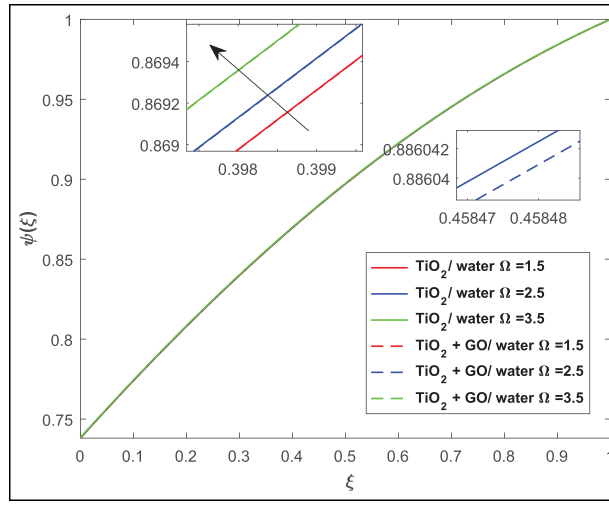

Figure 24. The impact of Ω over $\psi(\xi)$.

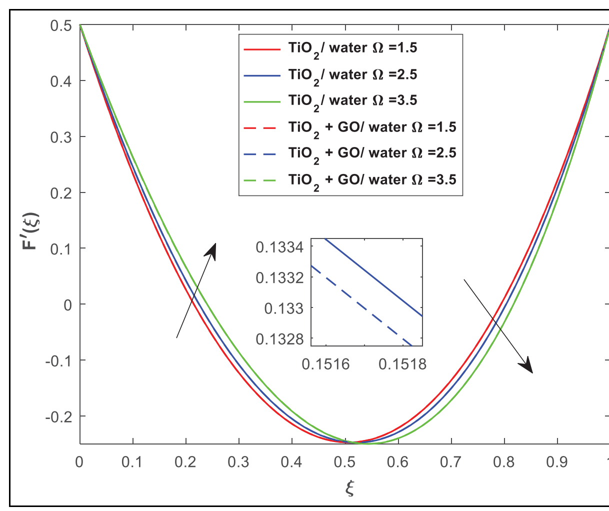

Figure 25. The impact of Ω over $F'(\xi)$.

in a thickening of the thermal boundary layer. The effects of rotational parameters Ω on the profile of $F'(\xi)$ and $F(\xi)$ velocities of hybrids nanofluid (TiO_2-GO)/water and nanofluid TiO_2/water are depicted in Figures 25 and 26. The function of Ω is becoming more dependent on $F'(\xi)$ and $F(\xi)$ velocities. Physically, The Coriolis force, which operates orthogonally to the velocity field and the rotational axis in a rotating channel, opposes the fluid's motion. Therefore, for $F'(\xi)$, a twofold impression is observed. When the velocity is amplified, the area near the lower disc experiences an increase in $F'(\xi)$, while the higher half of the disc gets a regression of this trend. It appears that the velocity $F(\xi)$ degrades for increasing values of 1. The effect of the rotation parameter Ω on tangential velocity $G(\xi)$ of hybrids nanofluid (TiO_2-GO)/water and nanofluid TiO_2/water is depicted in Figure 27. The rotation parameter has an increasing relationship with $G(\xi)$.

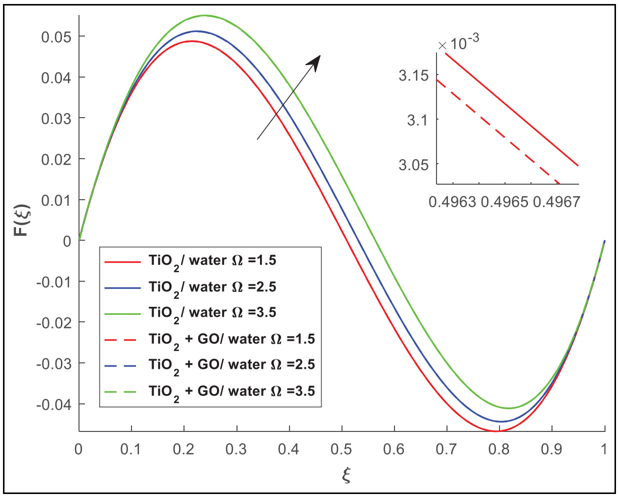

Figure 26. The impact of Ω over $F(\xi)$.

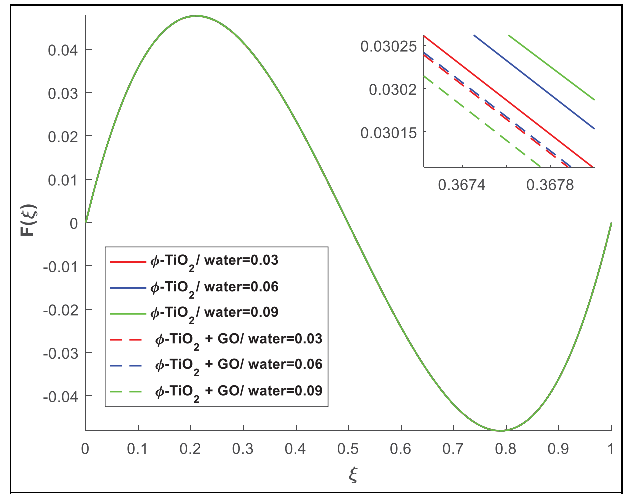

Figure 29. The impact of ϕ over $F(\xi)$.

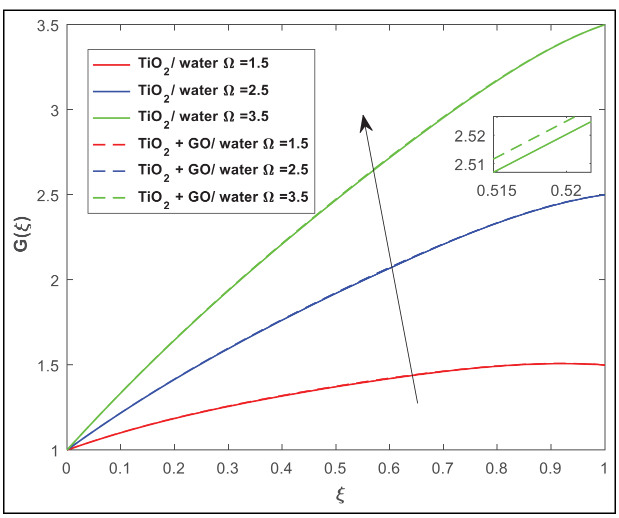

Figure 27. The impact of Ω over $G(\xi)$.

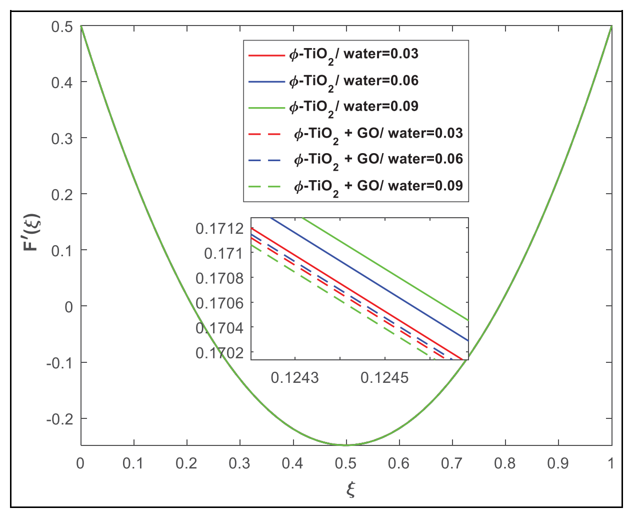

Figure 30. The impact of ϕ over $F'(\xi)$.

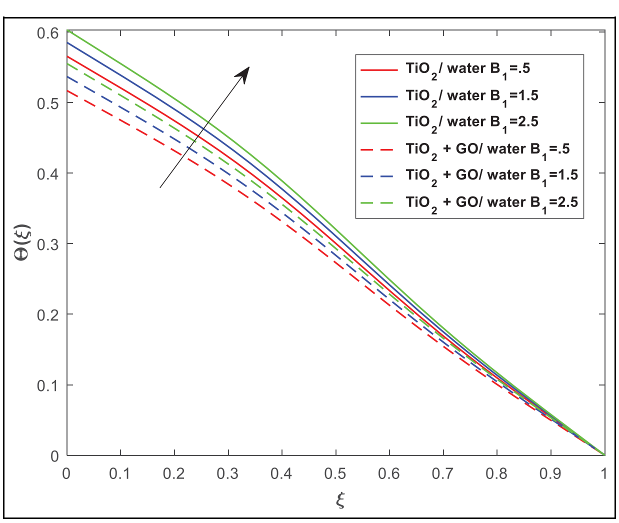

Figure 28. The impact of B_1 over $\theta(\xi)$.

Physically, higher Ω values cause the angular velocity to increase, and $G(\xi)$, therefore, has an increasing effect. The effects of the convective parameter B_1 on the temperature profile $\theta(\xi)$ of hybrids nanofluid (TiO_2-GO)/water and nanofluid TiO_2/water are depicted in Figure 28. The more is worth, the more $\theta(\xi)$. Physically, the thickness of the thermal boundary layer and the hydrodynamic boundary layer both increase as B_1 rises. Figures 29 to 31 shows the impact of nanoparticle volume fraction φ of hybrids nanofluid (TiO_2-GO)/water and nanofluid TiO_2/water on $F(\xi)$, $F'(\xi)$, and $G(\xi)$. On increasing volume fraction of each nanoparticle $TiO_2(\varphi_1)$ and $GO(\varphi_2)$ in equal quantity, the $F(\xi)$ and $F'(\xi)$ shows greater impact whereas tangential velocity shows decreasing impact. The increasing nanoparticle volume fraction in base fluid causes faster for the motion in axial and radial direction, because the addition of nanoparticle causes the outward movement of fluid,

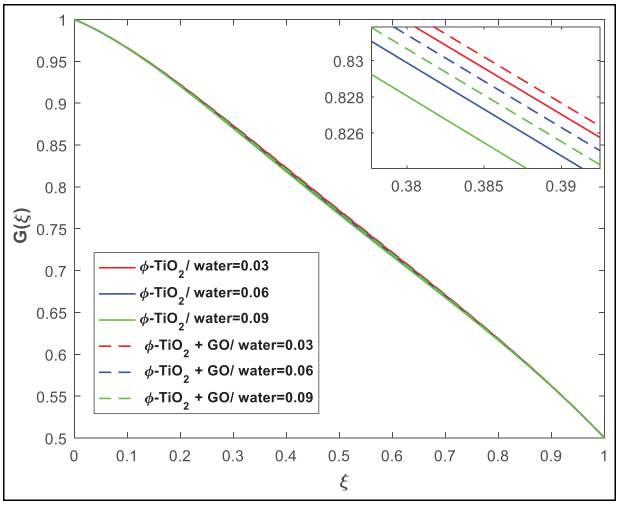

Figure 31. The impact of ϕ over $G(\xi)$.

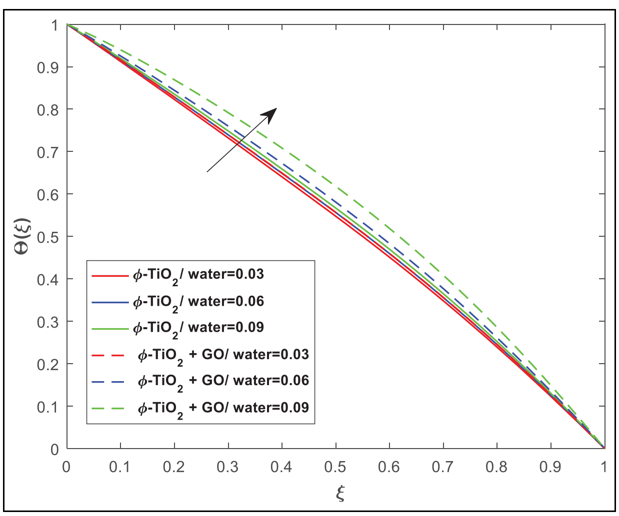

Figure 32. The impact of ϕ over $\theta(\xi)$.

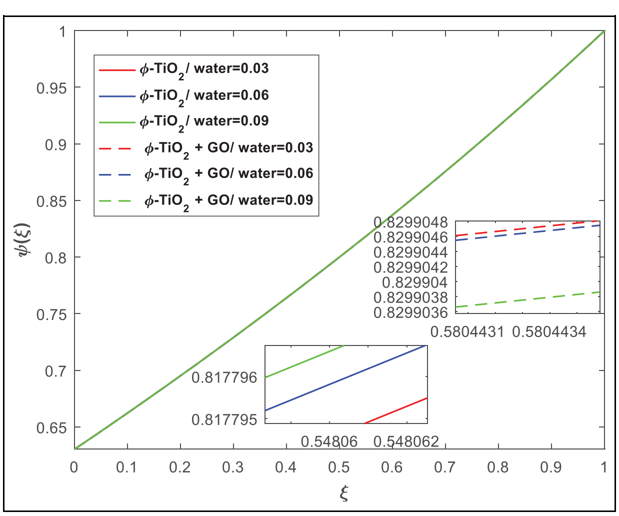

Figure 33. The impact of ϕ over $\psi(\xi)$.

Table 3. Different values of important parameter effects on the numerical results of Cf_{x1} and Cf_{x2}.

ϕ	Re	Ω	A_2	Ri	Cf_{x1} $(TiO_2-GO)/H_2O$	Cf_{x2} $(TiO_2-GO)/H_2O$
1.0					1.905723	1.603434
1.2					1.906534	1.608744
1.4					1.908445	1.612345
	0.2				1.890889	1.468723
	0.3				1.890865	1.461251
	0.4				1.890843	1.458723
		0.2			1.608343	0.545667
		0.4			1.524901	0.456743
		0.6			1.429834	0.334765
			0.3		1.347189	1.325664
			0.4		1.548946	0.768763
			0.5		1.750234	0.345400
				0.3	0.876534	0.876530
				0.4	0.876233	0.876226
				0.5	0.876021	0.876018

hence the velocities $F(\xi)$ and $F'(\xi)$ increases. On contrary, tangential velocity increase causes the hindrance for the motion in the tangential direction. Figure 32 shows how nanoparticle effect on temperature profile $\theta(\xi)$ of hybrids nanofluid (TiO_2-GO)/water and nanofluid TiO_2/water. On increasing volume fraction of each nanoparticle $TiO_2(\varphi_1)$ and $GO(\varphi_2)$ in equal quantity, the $\theta(\xi)$ shows greater impact. The rise in temperature can be attributed to the enhancement in the thermal conduction of hybrid nanofluid or nanofluid due to increase in the nanoparticles in the base fluid. Figure 33 shows how nanoparticle effect on concentration profile $\psi(\xi)$. On increasing volume fraction of each nanoparticle $TiO_2(\varphi_1)$ and $GO(\varphi_2)$ in equal quantity, the $\psi(\xi)$ raise with $TiO_2(\varphi_1)$ nanofluid but due to mixing of $TiO_2(\varphi_1)$ and $GO(\varphi_2)$ in base fluid, $\psi(\xi)$ falls. The reason for this behavior can be attributed to the fact the mixing of more nanoparticles causes the hybrid nanofluid or nanofluid to be more viscous and flow is resisted, hence $\psi(\xi)$ of nanoparticles falls. Significant effect of various parameters on Cf_{x1} and Cf_{x2}, Nu_{x1} and Nu_{x2}, and Sh_{x1} and Sh_{x2} for Titanium oxide (TiO_2) and Graphene oxide (GO) are examined in Tables 3 to 6. Table 3 examine the numerical values of the gradients of velocity Cf_{x1} and Cf_{x2} at both discs with $\phi, \mathrm{Re}, \Omega, Ri$ and A_2 parameters. Clearly, Cf_{x1} and Cf_{x2} are augments with ϕ and decreases with Re, Ri, Ω at both disc while, Cf_{x1} increases with A_2 at lower disc but decreases at upper disc. Table 4 examined the numerical values of the temperature Nu_{x1} and Nu_{x2} at both discs using a verity of parameters. Clearly, Nu_{x1} and Nu_{x2} are decreased at M, Ω, B_1, Rd while, increased with Ri at both disc. Table 5 examined the numerical values of rates of change of concentration Sh_{x1} and Sh_{x2} at both discs using a verity of parameters.

Table 4. Different values of important parameter effects on the numerical results of Nu_{x1} and Nu_{x2}.

M	B_1	Rd	Ω	Ri	Nu_{x1} $(TiO_2 - GO)/H_2O$	Nu_{x2} $(TiO_2 - GO)/H_2O$
1.5					1.890807	1.930805
1.6					1.890768	1.930769
1.7					1.890685	1.930688
	0.5				2.105689	1.105678
	0.6				1.905676	0.805667
	0.7				1.123409	0.113413
		1.1			0.564345	0.562022
		1.2			0.564219	0.561776
		1.3			0.564188	0.561476
			0.5		1.742133	1.862145
			0.6		1.705454	1.605423
			0.7		1.606565	1.603454
				0.5	1.447143	1.447143
				0.6	1.648943	1.648954
				0.7	1.850244	1.850244

Table 5. Different values of important parameter effects on the numerical results of Sh_{x1} and Sh_{x2}.

Ri	Sc	Cr	Sh_{x1} $(TiO_2 - GO)/H_2O$	Sh_{x2} $(TiO_2 - GO)/H_2O$
1.2			1.896576	1.613454
1.3			1.896543	1.608754
1.4			1.896456	1.597623
	0.5		1.908354	1.437645
	0.6		1.908465	1.438745
	0.7		1.908845	1.448776
		0.5	0.477165	0.355654
		0.6	0.605489	0.798755
		0.7	1.810254	1.345454

Clearly, Sh_{x1} and Sh_{x2} are increased at Sc and Cr while decreased with Ri at both disc. By contrasting the numerical values of $f''(0)$ and $-g'(0)$ in the limiting situation and changing the values of Ω, Table 6 is created to demonstrate the validity of our problem. Table 6 shows that there is a great deal of agreement between our numerical estimates and earlier literature Rawat et al.[63] and Khan et al.[64]

Conclusion

The current problem concerns the influence of a mixed convection MHD flow of a hybrid nanofluid (TiO_2-Go/water) as well as nanofluid (TiO_2/water) between two parallel and infinite spinning discs with joule heating and mixed convection in a porous medium in the presence of the magnetic field and radiation. The numerical solution is deduced by employing the "bvp4c" function in MATLAB. The influence of various key parameters, such as ϕ, M, A_1, A_2, B_1, Re, Ri, Sc, Ω and Cr. Some vital conclusions, is listed below.

- Radial velocity shows increasing behavior near the lower and upper disc for increasing values of the magnetic parameter and the mix convection parameter.
- The temperature profile rises as the magnetic, rotational, and convective parameters rise, as do the Eckert number and radiation parameter, while the mixed convection parameter falls.
- The concentration profile rises with the rotation parameter while falling with the chemical reaction parameter and Schmidt number.
- Increasing the radiation and magnetic parameters causes a decline in the heat transmission rate at both the upper and lower plates.
- The lower disc has a higher rate of heat transmission and mass transmission.

Table 6. The comparison of values $f''(0)$ and $-g'(0)$ for various values of Ω and the rest parameters are $\Pr = 6.2,\ \phi_1 = \phi_2 = M = B_1 = A_1 = A_2 = 0$.

Ω	Khan et al.[64] $f''(0)$	Rawat et al.[63] $f''(0)$	Present $f''(0)$	Khan et al.[64] $-g'(0)$	Rawat et al.[63] $-g'(0)$	Present $-g'(0)$
−1	0.06666314	0.06666303	0.06666301	2.0009522	2.00095213	2.00095209
−0.8	0.83942070	0.8394201	0.8394200	1.8025885	1.8025846	1.8025846
−0.3	0.1395088	0.1395088	0.1395087	1.3044236	1.30442355	1.30442321
0	0.09997221	0.09997221	0.09997221	1.0042776	1.0042756	1.00427551
0.5	0.06663419	0.06663416	0.06663412	0.5026135	0.50261344	0.502613432

Declaration of conflicting interests

The author(s) declared no potential conflicts of interest with respect to the research, authorship, and/or publication of this article.

Funding

The author(s) received no financial support for the research, authorship, and/or publication of this article.

ORCID iD

Amjid Rashid https://orcid.org/0000-0001-9174-298X

References

1. Abderrahmane A, Mourad A, Mohammed S, et al. Second law analysis of a 3D magnetic buoyancy-driven flow of hybrid nanofluid inside a wavy cubical cavity partially filled with porous layer and non-Newtonian layer. *Ann Nucl Energy* 2023; 181: 109511.
2. Krishna MV and Chamkha AJ. Hall and ion slip impacts on unsteady MHD convective flow of Ag-TiO_2/WEG hybrid nanofluid in a rotating frame. *Curr Nanosci* 2023; 19: 15–32.
3. Ishtiaq B, Zidan AM, Nadeem S, et al. Scrutinization of MHD stagnation point flow in hybrid nanofluid based on the extended version of Yamada-Ota and Xue models. *Ain Shams Eng J* 2023; 14: 101905.
4. Esfe MH, Kamyab MH, Mohammadnejad Ardeshiri E, et al. Study of MWCNT (40%) – CuO (60%)/10W40 hybrid nanofluid for improving laboratory oil performance by laboratory method and statistical response surface methodology. *Alex Eng J* 2023; 63: 115–125.
5. Gamachu D and Ibrahim W. Entropy production on couple-stress hybrid nanofluid flow in a rocket engine nozzle with non-Fourier's and non-Fick's law. *Ain Shams Eng J* 2023; 14: 101818.
6. Zainal NA, Nazar R, Naganthran K, et al. MHD flow and heat transfer of hybrid nanofluid over a permeable moving surface in the presence of thermal radiation. *Int J Numer Methods Heat Fluid Flow* 2021; 31: 858–879.
7. Zainal NA, Nazar R, Naganthran K, et al. Unsteady EMHD stagnation point flow over a stretching/shrinking sheet in a hybrid Al_2O_3-Cu/H_2O nanofluid. *Int Commun Heat Mass Transf* 2021; 123: 105205.
8. Anuar NS, Bachok N and Pop I. Influence of buoyancy force on Ag-MgO/water hybrid nanofluid flow in an inclined permeable stretching/shrinking sheet. *Int Commun Heat Mass Transf* 2021; 123: 105236.
9. Aladdin NAL, Bachok N and Pop I. Cu-Al_2O_3/water hybrid nanofluid flow over a permeable moving surface in presence of hydromagnetic and suction effects. *Alex Eng J* 2020; 59: 657–666.
10. Aladdin NAL and Bachok N. Boundary layer flow and heat transfer of Al_2O_3-TiO_2/water hybrid nanofluid over a permeable moving plate. *Symmetry* 2020; 12: 1064.
11. Khashi'ie NS, Md Arifin N, Pop I, et al. Melting heat transfer in hybrid nanofluid flow along a moving surface. *J Therm Anal Calorim* 2022; 147: 567–578.
12. Abu Bakar S, Md Arifin N, Khashi'ie NS, et al. Hybrid nanofluid flow over a permeable shrinking sheet embedded in a porous medium with radiation and slip impacts. *Mathematics* 2021; 9: 878.
13. Khashi'ie NS, Waini I, Zainal NA, et al. Hybrid nanofluid flow past a shrinking cylinder with prescribed surface heat flux. *Symmetry* 2020; 12: 1493.
14. Waini I, Ishak A and Pop I. Hybrid nanofluid flow towards a stagnation point on a stretching/shrinking cylinder. *Sci Rep* 2020; 10: 9296.
15. Khashi'ie NS, Hafidzuddin EH, Arifin NM, et al. Stagnation point flow of hybrid nanofluid over a permeable vertical stretching/shrinking cylinder with thermal stratification effect. *CFD Letters* 2020; 12: 80–94.
16. Elsaid EM and Abdel-wahed MS. Impact of hybrid nanofluid coolant on the boundary layer behavior over a moving cylinder: numerical case study. *Case Stud Therm Eng* 2021; 25: 100951.
17. Yahaya R, Arifin NM, Ali FM, et al. Nanoparticle shapes effects on MHD flow of hybrid nanofluid over a stretching/shrinking sheet with slip and chemical reaction. *J Nano Res* 2022; 75: 139–158.
18. Farooq U, Afridi M, Qasim M, et al. Transpiration and viscous dissipation effects on entropy generation in hybrid nanofluid flow over a nonlinear radially stretching disk. *Entropy* 2018; 20: 668.
19. Roşca NC, Roşca AV and Pop I. Axisymmetric flow of hybrid nanofluid due to a permeable non-linearly stretching/shrinking sheet with radiation effect. *Int J Numer Methods Heat Fluid Flow* 2021; 31: 2330–2346.
20. Khashi'ie NS, Arifin NM and Pop I. Unsteady axisymmetric flow and heat transfer of a hybrid nanofluid over a permeable stretching/shrinking disc. *Int J Numer Methods Heat Fluid Flow* 2021; 31: 2005–2021.
21. Khan U, Waini I, Ishak A, et al. Unsteady hybrid nanofluid flow over a radially permeable shrinking/stretching surface. *J Mol Liq* 2021; 331: 115752.
22. Shoaib M, Raja MAZ, Sabir MT, et al. Numerical analysis of 3-D MHD hybrid nanofluid over a rotational disk in presence of thermal radiation with joule heating and viscous dissipation effects using Lobatto IIIA technique. *Alex Eng J* 2021; 60: 3605–3619.
23. Wahid NS, Arifin NM, Khashi'ie NS, et al. Marangoni hybrid nanofluid flow over a permeable infinite disk embedded in a porous medium. *Int Commun Heat Mass Transf* 2021; 126: 105421.
24. Abbas N, Malik MY, Nadeem S, et al. On extended version of Yamada–Ota and Xue models of hybrid nanofluid on moving needle. *Eur Phys J Plus* 2020; 135: 1–16.
25. Waini I, Ishak A and Pop I. Hybrid nanofluid flow past a permeable moving thin needle. *Mathematics* 2020; 8: 612.
26. Waini I, Ishak A and Pop I. Hybrid nanofluid flow and heat transfer past a vertical thin needle with prescribed surface heat flux. *Int J Numer Methods Heat Fluid Flow* 2019; 29: 4875–4894.
27. Aladdin NAL, Bachok N and Pop I. Boundary layer flow and heat transfer of Cu-Al_2O_3/water over a moving horizontal slender needle in presence of hydromagnetic and slip effects. *Int Commun Heat Mass Transf* 2021; 123: 105213.

28. Puneeth V, Manjunatha S, Makinde OD, et al. Bioconvection of a radiating hybrid nanofluid past a thin needle in the presence of heterogeneous–homogeneous chemical reaction. *J Heat Transf* 2021; 143: 042502.
29. Reddy MG and Reddy KV. Influence of Joule heating on MHD peristaltic flow of a nanofluid with compliant walls. *Procedia Eng* 2015; 127: 1002–1009.
30. Maskeen MM, Zeeshan A, Mehmood OU, et al. Heat transfer enhancement in hydromagnetic alumina–copper/water hybrid nanofluid flow over a stretching cylinder. *J Therm Anal Calorim* 2019; 138: 1127–1136.
31. Khashi'ie NS, Arifin NM, Pop I, et al. Flow and heat transfer of hybrid nanofluid over a permeable shrinking cylinder with Joule heating: a comparative analysis. *Alex Eng J* 2020; 59: 1787–1798.
32. Yan L, Dero S, Khan I, et al. Dual solutions and stability analysis of magnetized hybrid nanofluid with joule heating and multiple slip conditions. *Processes* 2020; 8: 332.
33. Chamkha AJ, Dogonchi AS and Ganji DD. Magnetohydrodynamic flow and heat transfer of a hybrid nanofluid in a rotating system among two surfaces in the presence of thermal radiation and Joule heating. *AIP Adv* 2019; 9: 025103.
34. Li Z, Shafee A, Kandasamy R, et al. Nanoparticle transportation through a permeable duct with Joule heating influence. *Microsyst Technol* 2019; 25: 3571–3580.
35. Saranya S, Al-Mdallal QM and Javed S. Shifted Legendre collocation method for the solution of unsteady viscous-ohmic dissipative hybrid ferrofluid flow over a cylinder. *Nanomater* 2021; 11: 1512.
36. Al-Mdallal QM, Indumathi N, Ganga B, et al. Marangoni radiative effects of hybrid-nanofluids flow past a permeable surface with inclined magnetic field. *Case Stud Therm Eng* 2020; 17: 100571.
37. Renuka A, Muthtamilselvan M, Al-Mdallal QM, et al. Unsteady separated stagnation point flow of nanofluid past moving flat surface in the presence of Buongiorno's model. *J Appl Comput Mech* 2021; 7: 1283–1290.
38. Soomro FA, Haq RU, Al-Mdallal QM, et al. Heat generation/absorption and nonlinear radiation effects on stagnation point flow of nanofluid along a moving surface. *Results Phys* 2018; 8: 404–414.
39. Rashid I, Haq RU, Khan ZH, et al. Flow of water based alumina and copper nanoparticles along a moving surface with variable temperature. *J Mol Liq* 2017; 246: 354–362.
40. Al-Mdallal QM, Renuka A, Muthtamilselvan M, et al. Ree-Eyring fluid flow of Cu-water nanofluid between infinite spinning disks with an effect of thermal radiation. *Ain Shams Eng J* 2021; 12: 2947–2956.
41. Alhussain ZA, Renuka A and Muthtamilselvan M. A magneto-bioconvective and thermal conductivity enhancement in nanofluid flow containing gyrotactic microorganism. *Case Stud Therm Eng* 2021; 23: 100809.
42. Wahid NS, Arifin NM, Khashi'ie NS, et al. Hybrid nanofluid slip flow over an exponentially stretching/shrinking permeable sheet with heat generation. *Mathematics* 2020; 9: 30.
43. Rashidi MM, Abelman S and Freidooni Mehr N. Entropy generation in steady MHD flow due to a rotating porous disk in a nanofluid. *Int J Heat Mass Transf* 2013; 62: 515–525.
44. Raptis A, Perdikis C and Takhar HS. Effect of thermal radiation on MHD flow. *Appl Math Comput* 2004; 153: 645–649.
45. Ishak A, Nazar R and Pop I. Magnetohydrodynamic (MHD) flow and heat transfer due to a stretching cylinder. *Energy Convers Manag* 2008; 49: 3265–3269.
46. Rehman KU, Malik MY, Zehra I, et al. Group theoretical analysis for MHD flow fields: a numerical result. *J Braz Soc Mech Sci Eng* 2019; 41: 1–9.
47. Arikoglu A, Ozkol I and Komurgoz G. Effect of slip on entropy generation in a single rotating disk in MHD flow. *Appl Energy* 2008; 85: 1225–1236.
48. Nayak MK, Mehmood R, Makinde OD, et al. Magnetohydrodynamic flow and heat transfer impact on ZnO-SAE50 nanolubricant flow over an inclined rotating disk. *J Cent S Univ* 2019; 26: 1146–1160.
49. Mehmood A, Zameer A and Raja MAZ. Intelligent computing to analyze the dynamics of magnetohydrodynamic flow over stretchable rotating disk model. *Appl Soft Comput* 2018; 67: 8–28.
50. Barman T, Roy S and Chamkha AJ. Entropy generation analysis of MHD hybrid nanofluid flow due to radiation with non-erratic slot-wise mass transfer over a rotating sphere. *Alex Eng J* 2023; 67: 271–286.
51. Mahanthesh B, Gireesha BJ, Shehzad SA, et al. Nonlinear radiated MHD flow of nanoliquids due to a rotating disk with irregular heat source and heat flux condition. *Physica B* 2018; 537: 98–104.
52. Shamshuddin MD, Rao PS, Salawu SO, et al. Prevalence of secondary flow due to hall currents on radiative squeezing flow of a CuO-water nanofluid in a rotating channel: numerical prediction. *Proc IMechE, Part E: J Process Mechanical Engineering* 2022; 236: 1877–1888.
53. Salawu SO, Shamshuddin M and Anwar Bég O. Influence of magnetization, variable viscosity and thermal conductivity on Von Karman swirling flow of H_2O-Fe_3O_4 and H_2O-Mn-$ZNFe_2O_4$ ferromagnetic nanofluids from a spinning DISK: smart spin coating simulation. *Mater Sci Eng B* 2022; 279: 115659.
54. Shamshuddin M and Eid MR. Magnetized nanofluid flow of ferromagnetic nanoparticles from parallel stretchable rotating disk with variable viscosity and thermal conductivity. *Chin J Phys* 2021; 74: 20–37.
55. Khan MI, Alzahrani F and Hobiny A. Mathematical modeling and heat transfer in nanofluid flow of Newtonian material between two rotating disks. *Appl Nanosci* 2023; 13: 201–212.
56. Sreedevi P and Reddy PS. Effect of SWCNTs and MWCNTs Maxwell MHD nanofluid flow between two stretchable rotating disks under convective boundary conditions. *Heat Transf Res* 2019; 48: 4105–4132.
57. Gupta G and Rana P. Comparative study on Rosseland's heat flux on three-dimensional MHD stagnation-point multiple slip flow of ternary hybrid nanofluid over a stretchable rotating disk. *Mathematics* 2022; 10: 3342.
58. Zangooee MR, Hosseinzadeh K and Ganji DD. Hydrothermal analysis of MHD nanofluid (TiO_2-GO) flow between two radiative stretchable rotating disks using AGM. *Case Stud Therm Eng* 2019; 14: 100460.
59. Li YX, Muhammad T, Bilal M, et al. Fractional simulation for Darcy-Forchheimer hybrid nanoliquid flow with

partial slip over a spinning disk. *Alex Eng J* 2021; 60: 4787–4796.
60. Rafiq T, Mustafa M and Farooq MA. Modeling heat transfer in fluid flow near a decelerating rotating disk with variable fluid properties. *Int Commun Heat Mass Transf* 2020; 116: 104673.
61. Zhou SS, Bilal M, Khan MA, et al. Numerical analysis of thermal radiative Maxwell nanofluid flow over-stretching porous rotating disk. *Micromachines* 2021; 12: 540.
62. Chamkha AJ. MHD flow of a uniformly stretched vertical permeable surface in the presence of heat generation/absorption and a chemical reaction. *Int Commun Heat Mass Transf* 2003; 30: 413–422.
63. Rawat SK, Yaseen M, Khan U, et al. Significance of non-uniform heat source/sink and Cattaneo-Christov model on hybrid nanofluid flow in a Darcy-Forchheimer porous medium between two parallel rotating disks. *Front Mater* 2023; 9: 817.
64. Khan MI, Qayyum S, Hayat T, et al. Entropy generation minimization and statistical declaration with probable error for skin friction coefficient and Nusselt number. *Chin J Phys* 2018; 56: 1525–1546.

Appendix

Notation

$(r,\ \theta,\ z)$	Cylindrical coordinate system
B_0	Magnetic field strength (T)
C_f	Skin friction coefficient
c_p	Specific heat (J/kgK)
Cr	Chemical species
B_1	Convective parameter
g	Acceleration due to gravity (m/s^2)
Gr	Grashof number
p	Pressure (Pa)
h_1	Heat transfer coefficient of lower disc
A_1	Lower disc radial shrinkage rate
A_2	Upper disc radial shrinkage rate
k	Thermal conductivity $(W/m/K)$
M	Magnetic parameter
Ω	Rotation number
Ω_1	Bottom disc angular velocity
Ω_2	Higher disc angular velocity
Nu_x	Local Nusselt number
Re	Reynolds number
k_0^*	Mean absorption coefficient
σ_0^*	Stefan Boltzmann constant
T	Temperature of fluid (K)
T_1	Temperatures (lower disc)
T_2	Temperatures (lower disc)
t	Time (s)
α	Thermal diffusivity
β_T	Thermal expansion coefficient
ε_i	Stretching/shrinking parameter
r	Radial axes
θ	Tangential axes
Ri	Mixed convention parameter
μ	Dynamic viscosity (mPa s)
ν_f	Kinematic viscosity
Sc	Schmidt number
ρ	Density (Kg/m^3)
(ρc_p)	Heat capacity
σ	Electrical conductivity
τ_w	Shear stress
ϕ	Volume fraction of nanoparticles
ψ_B	Stream function

Subscripts

f	Base fluid
∞	Free-stream condition
nf	Nanofluid
ϕ	Volume fraction of nanoparticles
hnf	Hybrid nanofluid
(TiO_2)	Titanium di oxide
(GO)	Graphene oxide
Ri	Mixed convention parameter
μ	Dynamic viscosity (mPa s)